Prediction of permeability and formation factor of sandstone with hybrid lattice Boltzmann/finite element simulation on microtomographic images

WaiChing Sun[a,*], Teng-fong Wong[b]

[a] Department of Civil Engineering and Engineering Mechanics, Columbia University, New York, USA
[b] Earth System Science Programme, Faculty of Science, The Chinese University of Hong Kong, Hong Kong

ABSTRACT

In Fontainebleau sandstone, the evolution of transport properties with porosity is related to changes in both the size and connectivity of the pore space. Microcomputed tomography can be used to characterize the relevant geometric attributes, with the resolution that is sufficiently refined for realistic simulation of transport properties based on the 3D image. In this study, we adopted a hybrid computation scheme that is based on a hierarchical multi-scale approach. The specimen was partitioned into cubic sub-volumes for pore-scale simulation of hydraulic permeability and formation factor using the lattice Boltzmann method. The pore-scale results were then linked with finite element simulation in a homogenized scheme to compute and upscale the transport properties to specimen scale. The simulated permeability and formation factor have magnitude and anisotropy that are in good agreement with experimental rock physics data. Together with simulated and measured values of connected porosity and specific surface area, they provide useful insights into how pore geometry controls the evolution of the transport properties.

1. Introduction

The upper crust of the Earth is composed of rocks with a pore space made up of geometric features with very different morphology and scale, including relatively equant pores on the submicron scale and elongated fractures that may extend over hundreds of km. In most instances, these features are interconnected, thus constituting a percolative structure for hydraulic and electrical transport. A fundamental understanding of the transport properties of rock is of importance in many natural resources and environmental applications. Hydraulic permeability controls the migration, trapping, and extraction of conventional and unconventional hydrocarbon resources.[1] It influences contaminant transport, potential leakage of radionuclides in a waste repository, as well as the transient development and maintenance of excess pore pressure in hydrogeological settings.[2] Permeability may impact not only transport of pore fluid but also mechanical and failure behaviors in relation to the stability of a seismogenic system and induced seismicity.[3,4] Another transport property of importance is the electrical conductivity, which together with related AC properties such as induced polarization and streaming potential, provide useful geophysical tools for exploration in the oil and gas, as well as mining industries.

Both transport properties have been characterized in the rock physics laboratory under confining and pore pressures comparable to crustal settings. The electrical transport (characterized by the conductivity σ) is made up of two components: bulk conductivity σ_{bulk} through the pore fluid, and conductivity σ_s along the surface of the grains.[5] If the surface conduction component can be isolated from the overall conductivity σ, then the bulk conduction component can be identified. To decouple the effect of pore geometry from that of the electrolyte conductivity on the bulk conductivity of a rock saturated by a fluid of conductivity σ_w, one typically considers the formation factor: $F = \sigma_w / \sigma_{bulk}$, which has been observed to be related to the porosity (by Archie's law, an empirical power law). In contrast, the permeability k (which spans over 14 orders of magnitude in geomaterials) cannot be as simply related to the porosity, with the implication that other geometric attributes (such as pore size and connectivity) also exert important control over hydraulic transport.[5]

A fundamental understanding of transport properties would, therefore, hinge on a deeper understanding of the geometric complexity of the pore space. Traditionally, pore space in rock is imaged using optical and scanning electron microscopes. Supplementary information on the geometry of the pores and throats may also be gained from mercury porosimetry[6] and nuclear magnetic resonance (NMR) imaging.[7] Furthermore, recent advances in 3D imaging techniques such as laser scanning confocal microscopy (LSCM)[8] and X-ray computed

tomography (CT)[9] have provided enhanced perspectives on pore geometry complexity. Attributes such as pore dimension statistics, connectivity, and specific surface area can readily be characterized quantitatively.

In recent years, CT imaging has proved to be an effective tool in digital rock physics for probing both the mechanical and transport behaviors. In particular, for a clastic rock such as sandstone the void space is dominated by relatively equant pores connected by throats that are sufficiently large for direct imaging using X-ray microCT, and such data have elucidated the 3D geometric complexity[9] and its control over poromechanical properties[10–16] as well as mechanical failure and strain localization.[14,17–20] The first such attempts in digital rock physics were by Spanne et al.[21] and Auzerais et al.[22] who acquired CT images with a synchrotron X-ray source and analyzed the geometric attributes and transport properties of Fontainebleau sandstone samples with nominal porosities of 19.7% and 15.2%, respectively.

Fontainebleau sandstone is monomineralic and does not show significant variability in quartz grain size or sorting. However, it has a wide variability in porosity (2–30%) attributed to different degrees of silicification during its diagenetic evolution.[23] A systematic study of its acoustic and transport properties and their dependence on porosity was conducted by Jacquin[24] and Bourbie and Zinszner,[25] who observed that the relation between hydraulic permeability and porosity undergoes a transition from high to low porosities. Above a crossover porosity of ~9%, the permeability and porosity are related by a power law with a constant exponent of ~3.05. Below this crossover, permeability decreases drastically with decreasing porosity, manifested by an exponent value up to 7.3. This significant reduction of permeability in the low-porosity regime is attributed to the corresponding decrease in pore connectivity that ultimately leads to the percolation threshold at a porosity of ~4%.[26,27] Since then, Fontainebleau sandstone has been the focus of extensive research in both experimental and digital rock physics for several decades. Nevertheless, there remain a number of outstanding questions, such as the discrepancies between calculated and measured effective permeabilities, relationships between formation factor and permeability under different porosities, and effects of microstructural attributes, such as pore size distribution, pore connectivity and effective hydraulic radius, on the porosity-permeability relationship.[13,28–31] The objective of the present study is to revisit some key issues related to hydraulic and electrical transport.

To probe the physics behind the contrast in permeability evolutions between the high- and low-porosity regimes in Fontainebleau sandstone, Lindquist et al.[9] used a synchrotron X-ray source to image the pore spaces of four samples with nominal porosities 7.5%, 13%, 15% and 22%, respectively. They quantitatively analyzed the pore geometry, and furnished the segmented data to Arns et al.[34] for computation of the formation factors, which showed good agreement with experimental measurements. Arns et al.[35] followed up with computation of permeability using the lattice Boltzmann (LB) method. Whereas the agreement between the simulated and laboratory data was reasonable in the high-porosity regime, it was not as satisfactory for the sample with 7.5% porosity, with a variability of 2 orders of magnitude in the LB simulated permeability. This discrepancy is suggested to be related to a combination of image resolution and discretization effects in Arns et al..[35] However, in a parallel study, Thovert et al.[36] investigated another Fontainebleau sandstone sample of porosity 6.92%, that had been scanned at a comparable resolution. In contrast, the analysis in Thovert et al.[34] on the geometry, percolation and electrical conductivity seemed to indicate that the image resolution in [35] could be adequate.

A robust simulation in the low-porosity regime of the permeability and connectivity loss is key to understanding how pore geometry, percolation and transport evolve with diagenesis in a sedimentary rock. In recent years, there have been significant advances in both X-ray CT imaging and numerical computation. If indeed image resolution of Lindquist et al.[9] is inadequate for permeability simulation in this regime, one may readily acquire new CT data for the sample at a more

refined resolution with current facilities. Meanwhile, leveraging recent advances in computational poromechanics such as [15 and 16] to analyze this rather unique set of digital rock physics data may also bring new insights and clarification. Furthermore, comprehensive experimental studies of Fontainebleau sandstone[29] have recently been undertaken, which may lead to further understanding of the constraints and potential issues on the simulation-based digital rock technology related to geometrical attributes, image resolutions and other numerical issues.

Our computation scheme is based on a hierarchical multi-scale approach.[15,16,37] The specimen was partitioned into small representative elementary volumes (REV) for pore-scale calculation of transport properties. Unlike previous studies that used different numerical techniques (e.g. LB method for permeability and finite difference method for formation factor), we here employed LB simulations for both types of transport, which may provide a more consistent basis for synthesizing permeability, formation factor and geometric attributes. The pore-scale LB results were then linked with finite element (FE) simulation in a homogenized scheme to compute formation factor and permeability tensor at specimen-scale.

2. Numerical analysis

2.1. Fontainebleau sandstone and X-ray CT imaging

The Fontainebleau sandstone data set was presented by Lindquist et al.[9] who characterized cylindrical samples (diameter 4.52 mm) of the same length cored from 4 blocks of measured porosities 7.5%, 13%, 15% and 22%. X-ray CT imaging was performed at the X2-B beam line of the National Synchrotron Light Source at Brookhaven National Laboratory. With a linear voxel size of 5.7 μm in all three directions, the $795 \times 795 \times 512$ reconstructed image sections were padded to a volume of $800 \times 800 \times 512$ voxels.

The images were encoded in 8 bits (0 − 255). Lindquist et al.[9] used an indicator Kriging algorithm to segment the CT data, and this binary data set of Fontainebleau sandstone has been widely used in computational studies.[32–35] Nevertheless, in this study we did not adopt this binary data set, but instead started with the 8-bit data. In parts of the data for the 15% porosity sample, we observed "ring" artifacts, that may have been induced by slight differences in the column-by-column response of the CCD detectors, with resultant small variations in grey level that got propagated through the data sets during the reconstruction and appear in cross-sectional images as rings.[11] Accordingly, we decided not to include this sample in this study, and simply focused on CT data for the three samples FB75, FB13 and FB22 with total porosities of 7.5%, 13%, and 22%, respectively. In this study, segmentation of the data was performed using the default option of the auto-thresholding module of the software ImageJ, which is a variation of the IsoData algorithm for two-phase segmentation proposed by Ridler and Calvard.[38] This modulus is selected after visual inspections of the binary images generated from all 16 algorithms available in ImageJ. Geometrical attributes were then extracted from the segment images; a flood-filled algorithm was adopted to identify the connected porosity, and Crofton formula was used to characterize the surface area. Details of the flood-filled algorithm and the Crofton formula can be found in [39,40].

2.2. Estimation of effective permeability and formation factor via hybrid lattice Boltzmann/finite element simulations

In this work, effective permeability and formation factor were calculated using a hybrid lattice Boltzmann/finite element (LB/FE) scheme as a cost-efficient alternative to direct numerical simulations.[15,16,28,37] In the hybrid scheme, we first use a region growing algorithm to distinguish the isolated pore space from the connected one. Then, the connected pore space of a numerical specimen is divided into cubic unit cells of identical sizes ($190 \times 190 \times 190$ voxels, with volume of $(1.08 \text{ mm})^3$); within each unit cell made up of, a Poisson problem and

Navier-Stokes problem were solved via the LB method to compute its formation factor and permeability, respectively.

Fredrich et al.[11] have provided a comprehensive review of the use of LB method for voxel-based calculation of permeability in porous rock. In this study, the effective permeability of unit cell was estimated using a conventional LB solver with 3-D 19-speed (D3Q19) lattices and BGK relaxation collision operator. Sun et al.[16,37] have presented details of the numerical methodology, which we briefly summarize here. According to the single-relaxation-time BGK approximation, the evolution of the distribution function f_i along the direction $\mathbf{e_i}$ within one time step (from t to $t + \delta t$) is defined as:

$$f_i(\mathbf{x} + \mathbf{e_i}, \ t + \delta t) - f_i(\mathbf{x}, \ t) = -\frac{1}{\tau}(f_i(\mathbf{x}, \ t) - f_i^{eq}(\mathbf{x}, \ t)) \tag{1}$$

where f^{eq} is the truncated Maxwell-Boltzmann equilibrium distribution function and τ is the single-relaxation time. For the standard BGK model, this equilibrium distribution function takes the following form,

$$f_i^{eq}(\mathbf{x}, t) = \rho w_i \left(1 + \frac{3\mathbf{e_i} \cdot \mathbf{v}}{c^2} + \frac{9(\mathbf{e_i} \cdot \mathbf{v})^2}{2c^4} - \frac{3(\mathbf{v} \cdot \mathbf{v})^2}{2c^2} \right) \tag{2a}$$

where w_i is the weight value that depends on the lattice geometry chosen for the LB simulations, and c is the speed of sound. The macroscopic velocity $\mathbf{v}$ and density ρ are related to the distribution function f_i, i.e.,

$$p = c^2 \rho, \quad \rho = \Sigma_{i=1}^N f_i, \quad \mathbf{v} = \frac{1}{\rho} \Sigma_{i=1}^N f_i \mathbf{e_i} \tag{2b}$$

where p is the pore pressure. We conducted LB simulations with pressure gradients applied in three orthogonal directions across opposite faces of the unit cell, from which we can infer the permeability tensor by measuring Darcy's velocity while prescribing pressure gradient. This method of imposing pressure gradient is first introduced by Zou and He.[41] Due to the ideal gas equation of the state and constant speed of sound, one may prescribe the pressure gradient by simply imposing a density difference at the two opposite faces. In this case, the fluid in the pore space is not strictly speaking incompressible. It should be noted that this is not the only way to construct the inverse problem for permeability calculation. For instance, one may impose external body force or force density applied in the sample volume. Recent work, such as Narvaez Salazar and Harting[42] nevertheless find that the estimated permeability obtained from the force density approach can be strongly dependent on the effective length of the specimen and hence not recommended.

In this study, we also calculated the formation factor, which requires the solution of the Poisson's equation instead of the steady solution of the Navier-Stokes equation. The simplest way to tackle this is to modify the above BGK solver originally linked to the macroscopic Naiver-Stokes equation so that it gives instead solution of the Poisson equation at steady state. As pointed out by previous studies [e.g., 43,44, this can readily be achieved by rewriting the truncated Maxwell-Boltzmann equilibrium distribution function, such that the higher-order terms $O(v^2)$ are all neglected. By setting $c = 1$, the equilibrium distribution function reduces to,

$$f^{eq}(\mathbf{x}, \ t) = \rho w_i(1 + 3\mathbf{e_i} \cdot \mathbf{v}) \tag{3a}$$

Such a model would recover the diffusion equation with an isotropic diffusivity associated with each voxel of the void space that is given by[46]:

$$D = \frac{(\tau - \frac{1}{2})}{3\delta t} l^2 \tag{3b}$$

where l is the voxel length and τ is the single-relaxation time. The formation factor then corresponds to the ratio between the resistivity of the sample obtained from the solution of the Poisson's equation and that of the pore fluid. The diffusion solver also uses the D3Q19 lattices, although previous work such as [44] have shown that a D3Q15 could be

sufficient. We use the so-called on-grid bounce-back algorithm to model the no-slip conditions on the pore-solid boundary. Due to the one-side treatment on the steaming at the boundary, the boundary condition is only first-order accurate. It should be noticed that the mid-grid bounce-back algorithm is second-order accurate. However, such a technique would require the introduction of fictitious nodes placed in between the closest lattice nodes and the solid wall and therefore more difficult to use for porous media of more complex pore geometry.

Having calculated the orthogonal components of the permeability and formation factor of each of the 24 unit cells, the overall effective permeability and formation factor of the three numerical specimens (each made up of $2 \times 2 \times 2$ unit cells) were computed by solving the macroscopic diffusion problem (neglecting body forces) via the FE method. For hydraulic transport, the local permeabilities of the unit cells estimated from the LB simulations were assigned to the Gauss points of each finite element associated with the corresponding unit cell, leading to a heterogeneous permeability field discretized by the finite element meshes. To compute the overall permeability, the following governing equation was solved numerically with approximate boundary conditions:

$$v_{j,j} = 0 \text{ in } \Omega^s \text{ (continuity equation)} \tag{4a}$$

$$v_i = -\frac{k_{ij}}{\mu} p_j \text{ in } \Omega^s \text{ (Darcy's law)} \tag{4b}$$

where v is Darcy's velocity, μ is the dynamic viscosity, p is the pore pressure, Ω^s is the finite element domain. By assuming that the permeability tensor is symmetric, the six independent components of the locally homogenized effective permeability tensor k_{ij} can be computed by applying different boundary conditions on the same numerical specimen. By relating volume averaged velocity $< v_i(x) >$ with the prescribed macroscopic pressure gradient $p_{,j}$ the effective permeability k_{ij} can be recovered via Darcy's law, i.e.,

$$k_{ij} = - < v_i > \frac{\mu}{p_j} \tag{5}$$

Notice that the macroscopic effective permeability is sometime directly inferred from volume averaging or geometric averaging. For instance, Sun et al.[45] compared the geometrical averaged, volume averaged permeabilities with the calculated permeability from finite element inverse problem and found that the results from geometric averaging is often closer to the finite element calculation for samples with notable spatial variability. Nevertheless, this conclusion is likely restricted to isotropic or slightly anisotropic materials, such as the Fontainebleau sandstone. For highly anisotropic materials, the eigenvalues and spectral directions of the permeability tensor must be considered carefully when calculating the volume and geometrical averaged permeability tensors.

The calculation of the specimen-scale formation factor follows the same procedure, except that (1) it is the effective diffusivity, not the effective permeability of the unit cell is assigned to the Gauss points of finite elements, and (2) the macroscopic finite element model will also solve the Poisson equation, which takes the same form as the diffusion problem. Since computations of local effective permeability and formation factor can be carried out independently and simultaneously, this multi-scale approach is easy to implement and its performance can be greatly enhanced in a parallel computing environment.

3. Simulated data

We will first present the pore-scale LB simulations on the 24 cubic sub-volumes, which have computed porosities ranging from 6.5% to 21.1%. Permeability and formation factor were calculated for hydraulic and potential gradient applied along the axial direction. Pore geometry and flow behavior in the low-porosity sample FB 75 were observed to be fundamentally different from the other two samples (FB13 and
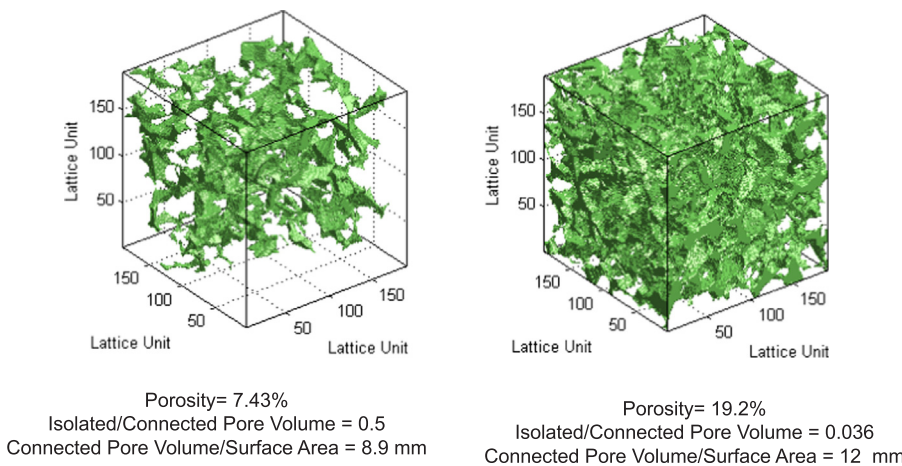
Fig. 1. MicroCT images of sub-volumes of FB75 and FB22. The pore space corresponds to the opaque portion of the segmented image. (a) For this cubic unit cell of FB75, the computed porosity is 7.4%, isolated/ connected pore volume = 0.5, and hydraulic radius (connected pore volume/surface area) = 8.9 μm. (a) For this cubic unit cell of FB22, the computed porosity is 19.2%, isolated/ connected pore volume = 0.036, and (b) hydraulic radius (connected pore volume/ surface area) = 12 μm.

Porosity= 7.43%
Isolated/Connected Pore Volume = 0.5
Connected Pore Volume/Surface Area = 8.9 mm

Porosity= 19.2%
Isolated/Connected Pore Volume = 0.036
Connected Pore Volume/Surface Area = 12 mm

Porosity= 7.43%
k = 0.0316 darcy; FF = 332
Isolated/Connected Pore Volume = 0.5
Connected Pore Volume/Surface Area = 8.9 μm

Porosity= 19.2%
k = 3.08 darcy; FF = 8.5
Isolated/Connected Pore Volume = 0.036
Connected Pore Volume/Surface Area = 12 μm
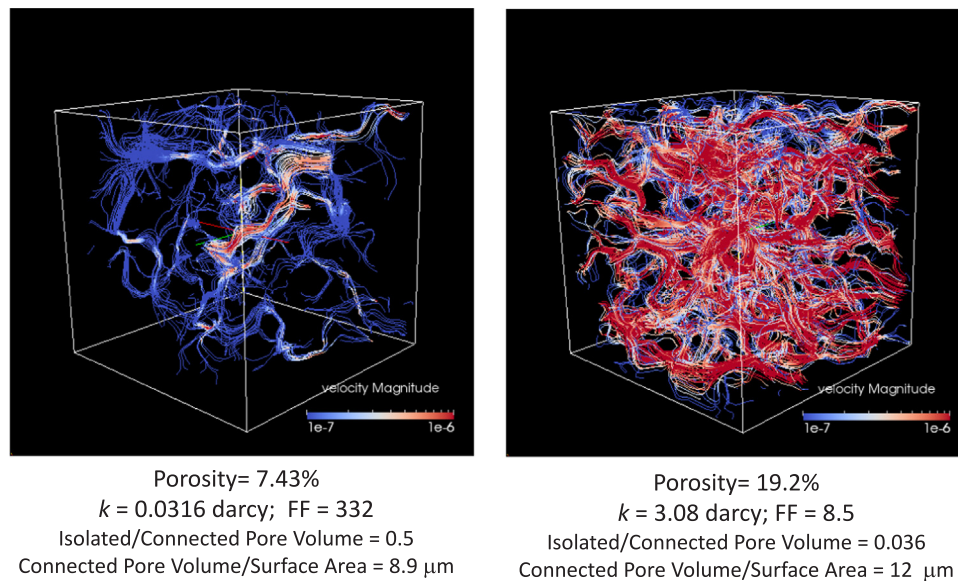
Fig. 2. Streamlines of hydraulic transport from LB simulations. Pore structure of two cubic units was shown in Fig. 2. Pressure gradient was in the axial direction. (a) The flow is localized along a few preferential paths which are tortuous. Simulated permeability and formation factor are $3.16 \times 10^{-14} m^2$ and 332, respectively. (b) The flow is distributed among multiple paths in a relatively homogeneous pattern. Simulated permeability and formation factor are $3.08 \times 10^{12} m^2$ and 8.5, respectively.

FB22). Whereas the total and connected porosities in the latter are basically identical; a significant portion of the pore space in FB75 is unconnected. As an example, in the unit cube of FB75 shown in Fig. 1a, ratio of the isolated to connected porosity is about 0.5. In comparison, the unit cube of FB22 in Fig. 1b has an almost negligible ratio of 0.036. Whereas the flow in the samples FB13 and FB22 (Fig. 2b) is distributed among multiple paths in a relatively homogeneous pattern, the flow in FB75 is typically localized along a few preferential paths which are tortuous (Fig. 2a), with the implication that connectivity has decreased significantly in many parts of this sample. Analogous development of preferential paths was analyzed by David[47] using a network model of the pore space.

The simulated values of permeability and formation factor are plotted as functions of computed total porosity in Figs. 3 and 4, respectively. For reference, compiled laboratory data for permeability[6,29,48,49] and formation factor[29,45,49,50] are included in these figures. The simulated permeability of sub-volumes of FB13 and FB22 evolves with porosity following the relatively gradual trend delineated by laboratory data in the high-porosity regime. In contrast, the simulated permeability of FB75 decreases drastically with porosity decrease, in agreement with the overall trend of the laboratory data in the low-porosity regime.

The connected and total porosities are compared in Fig. 5. For each unit cube of FB13 and FB22, total porosity is typically larger than the connected porosity, but the difference is typically very small. In contrast, the difference between total and connected porosities is significant in each subvolume of FB75. There is an overall trend for this difference to increase with decreasing porosity. For reference, we include the laboratory measurements of 51 in Fig. 5. There is good agreement between the measurements and values we derived from the binary CT data.

The specific area is given by the ratio between the surface area and volume of the pore space. Its reciprocal provides a characteristic length, and if one specifies the volume to be the connected part of the pore space that can be wetted by a fluid, then this length corresponds to the "hydraulic radius".[52,53] Since we have derived both connected volumes and surface areas directly from the segmented CT images, the characteristic lengths can be determined from their ratios, which are plotted in Fig. 6. Lengths so inferred from our CT data are on the order of 10 μm, and there seems to be an overall trend for the hydraulic radius to slightly decrease with porosity reduction. For comparison, we include in Fig. 6 the stereological measurements of 46 on 2D thin-sections of
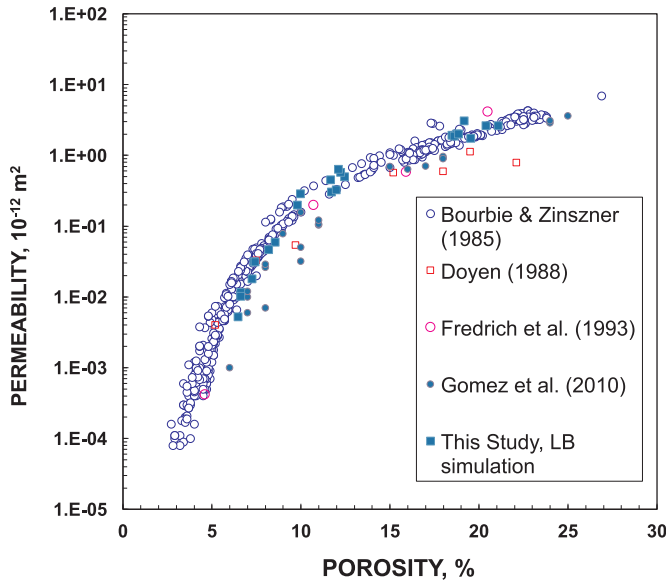
Fig. 3. Permeability of Fontainebleau sandstone as a function of porosity. Simulated values from this study (with pressure gradient along the axial direction) are shown as solid squares. For comparison, laboratory data from the following studies are also plotted: Bourbie and Zinszner,[25] Doyen,[48] Fredrich et al.,[49] and Gomez et al.[29].
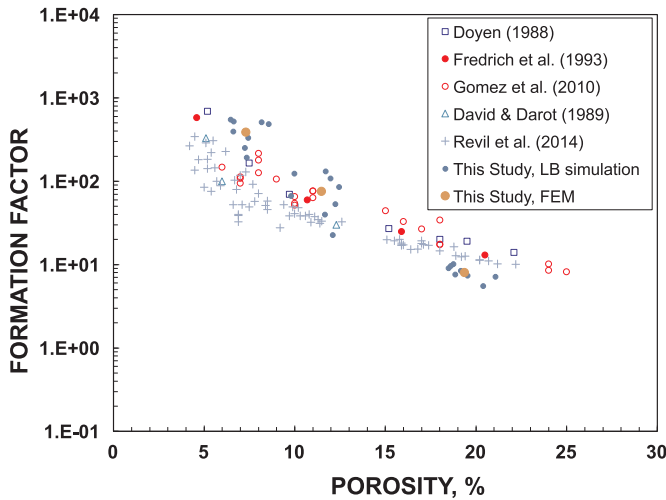

Fig. 4. Formation factor of Fontainebleau sandstone as a function of porosity. Values from this study from LB and FE simulations are shown as blue and brown circles, respectively. For comparison, laboratory data from the following studies are also plotted: Doyen,[48] David and Darot,[50] Fredrich et al.,[49] and Gomez et al.[29].

four samples, NMR diffusion measurements of [54] for two samples, and mercury porosimetry data of [29] for three samples.

We also conducted LB simulations with pressure gradients applied in three orthogonal directions, from which one can infer the permeability tensor. We plot in Fig. 7a the three principal permeabilities derived from such computations. Permeability anisotropy is not pronounced, especially in subvolumes from the two porous samples FB13 and FB22. To characterize the anisotropy, we followed Clavaud et al.[55] who introduced the "quadratic deviation" defined as follows:

$$I = \left[\frac{(K_1 - \overline{K})^2 + (K_2 - \overline{K})^2 + (K_3 - \overline{K})^2}{K_1^2 + K_2^2 + K_3^2} \right]^{1/2} \tag{6}$$

We assume that the effective permeability tensor is symmetric and positive definite. As a result, the eigenvalues of the permeability tensor
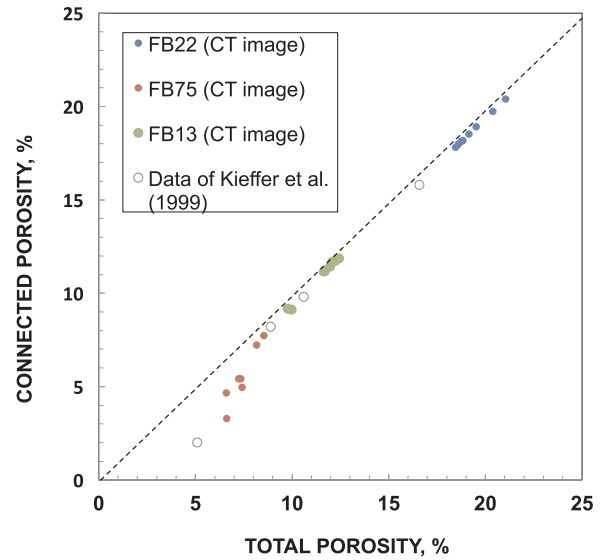

Fig. 5. Connected porosity as a function of total porosity. Computed values for all 24 cubic unit cells are shown as solid circles. For comparison, laboratory measurements of Kieffer et al.[51] are also shown.
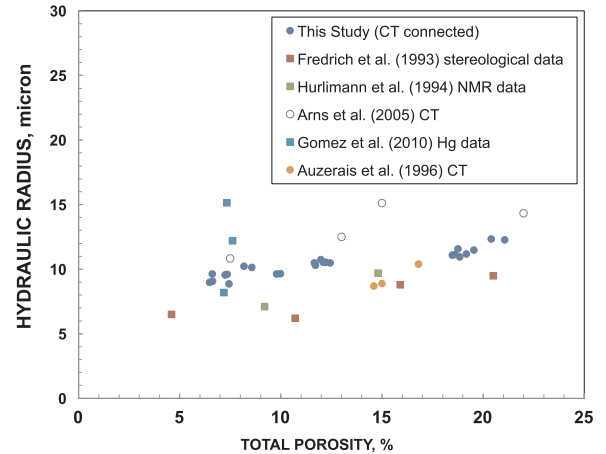

Fig. 6. Computed Hydraulic radius as function of total porosity. Values we inferred from the CT images of the 24 cubic unit cells are shown as blue circles. For comparison, stereological measurements of Fredrich et al.[49] on 2D thin-sections, NMR measurements of Hürlimann et al.[54], and mercury porosimetry data of Gomez et al.[29] are plotted. We also include values inferred from CT images by Auzerais et al.[22] and Arns et al.[28].

are identical to the principal values. Here we denote the major, immediate and minor principal permeabilities as K_1, K_2 and K_3. where $K_1 \geq K_2 \geq K_3$, and denote the geometrical mean as $\overline{K} = (K_1 K_2 K_3)^{1/3}$, respectively. The values we determined from the LB simulations are plotted versus porosity in Fig. 7b. Unit cubes of FB13 and FB22 have relatively small I values of 0.2 or less. The values are higher by a factor of 2 in FB75, probably related to the development of highly tortuous, preferential paths. Because Fontainebleau sandstone is not associated with appreciable bedding, one rarely attempts to characterize in the laboratory its permeability anisotropy, which is expected to be relatively small. We include in the figure one such measurement by Clavaud et al.[55] inferred from X-ray tomography monitoring during the displacement of a salty tracer. Their inferred I value falls near the high end of our simulated values. It should be noted that there are other anisotropy parameters that one can use instead of I, which was adopted here simply because it allows us to directly compare our simulations with the experimental value of [55].

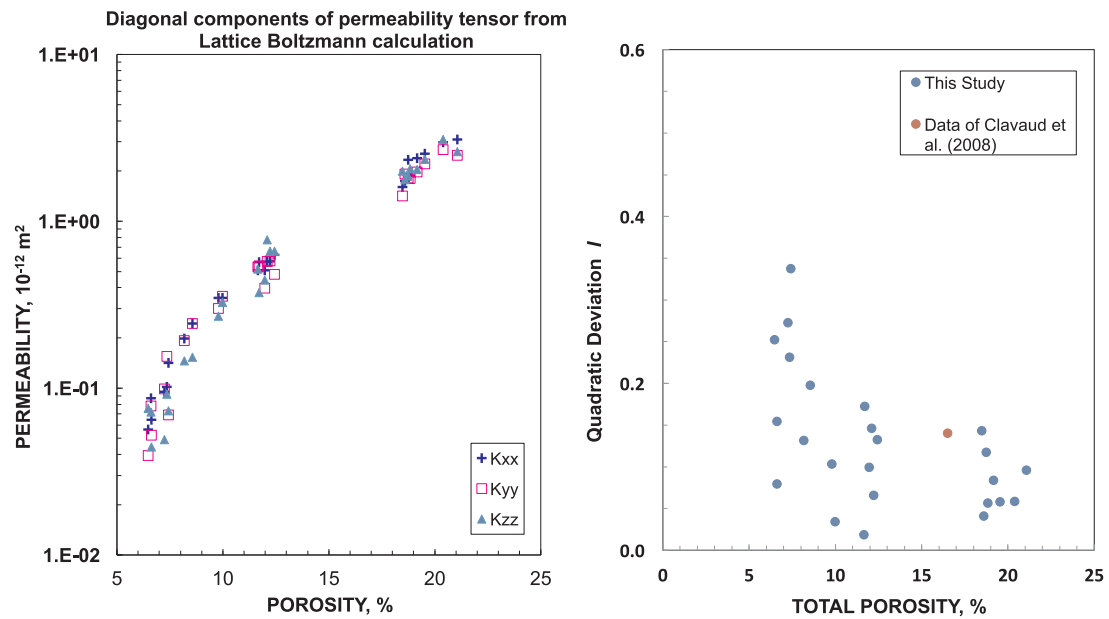Finite element simulations based on our homogenized scheme show

Fig. 7. (a) Simulated permeability of Fontainebleau sandstone as a function of porosity. LB simulations were conducted on the 24 cubic unit cells with pressure gradients applied in three orthogonal directions. (b) Anisotropic permeability values of the 24 cubic units were substituted into Eq. (6) to calculate the quadratic deviation, plotted here as a function of total porosity. For comparison, laboratory measurement of Clavaud et al.[55] is also included.

(a) Porosity 22%
Permeability (isotropic) = 2.01 Darcy
Formation Factor = 8.03

(b) Porosity 13%
Permeability (isotropic) = 0.497 Darcy
Formation Factor = 76

(c) Porosity = 7.5%
Permeability (isotropic) = 0.116 Darcy
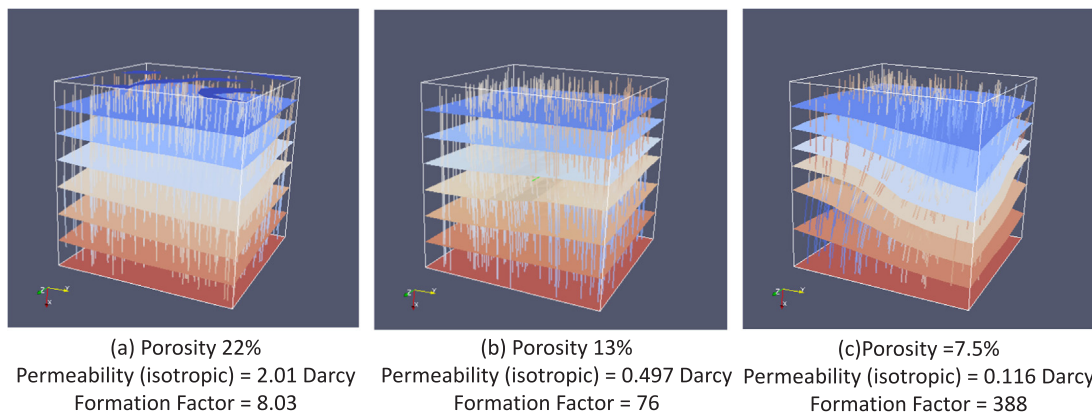Formation Factor = 388

Fig. 8. Streamlines of the homogenized hydraulic transport from FE simulation of specimens (a) FB22, (b) FB13, and (c) FB75 LB. Each numerical specimen was made up of $2 \times 2 \times 2$ cubic unit cells. Whereas the overall flow pattern is relatively homogeneous in both samples FB13 and FB22, that in FB75 shows significant heterogeneity and tortuosity.

Table 1
Comparison of permeability and formation factors inferred from lattice Boltzmann simulations performed on three tomographic images of Fontainebleau sandstone.

Name Tag	Connected Porosity	Total Porosity	Formation Factor	Permeability FEM full tensor, mD	Permeability FEM scalar, mD	Permeability GAVG, mD	Permeability VAVG, mD
FB75	5.16E − 02	7.31E − 02	3.88E + 02	3.95E + 01	1.16E + 02	8.04E + 01	8.79E + 01
FB13	1.09E − 01	1.15E − 01	7.60E + 01	1.62E + 02	4.97E + 02	4.74E + 02	5.03E + 02
FB22	1.87E − 01	1.94E − 01	8.03E + 00	7.07E + 02	2.27E + 03	2.22E + 03	2.25E + 03

an overall homogeneous flow pattern in both samples FB13 and FB22 (Fig. 8a, b). In contrast, the flow field in FB75 shows more profound heterogeneity and effective tortuosity (Fig. 8c). The estimated permeability inferred from LB/FE simulations and from volume-averaging (denoted as V AVG) and geometric-averaging (denoted as G AVG) unit cells are compiled in Table 1. As shown in Fig. 9, we found a consistent trend where the estimated permeabilities inferred from volume-averaging, geometric-averaging and LB/FE simulations are very close for high-porosity samples but the discrepancy becomes more significant when the porosity is low. This observed trend indicates that the spatial variability of the local permeability is likely to be higher, as the

porosity reduction is likely to be not uniform.

4. Discussion

The progressive development of cementation in Fontainebleau sandstone has resulted in a decrease of pore and throat sizes, as well as subtle changes in connectivity. Relevant geometric attributes of its pore space are accordingly modified, which are manifested by corresponding changes in both the hydraulic and electrical transport properties. Even though X-ray CT imaging can now resolve fine details of the pore geometry, to realistically simulate the evolution of permeability and
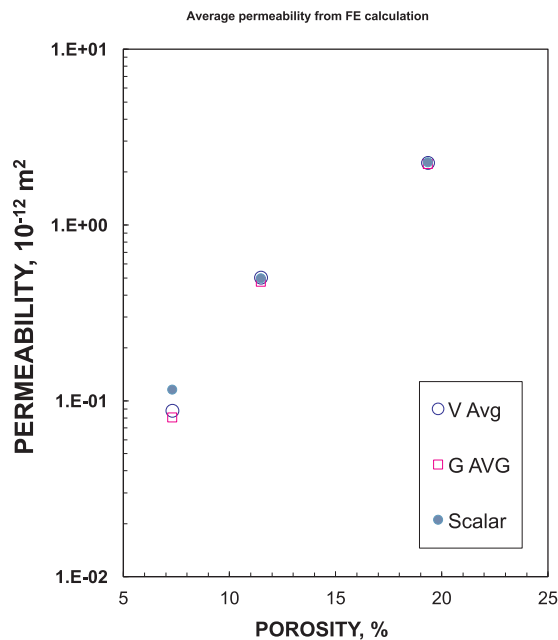
Fig. 9. Average permeabilities of the three specimens FB22, FB13, and FB75 LB computed by the homogenized FE scheme. For each specimen, three different averages were obtained using the different schemes described in the text.

formation factor with porosity in Fontainebleau sandstone has remained a challenge in digital rock physics, especially with regard to the progressive loss of connectivity in the low-porosity regime.

4.1. Digital rock physics

In this study, we have adopted a hierarchical multi-scale approach[15,16,37] to simulate hydraulic and electrical transport in three samples of Fontainebleau sandstone that had been imaged using X-ray CT by Lindquist et al.[9] Each specimen was partitioned into 8 unit cubes with linear dimensions of 1.08 mm for pore-scale LB calculation of permeability and formation factor. The image resolution seems adequate, and there is not a need to acquire CT images at a more refined resolution for such digital rock physics applications, in agreement with the analysis of [36] that focused on the percolation and electrical conductivity.

Unlike previous studies that used different numerical techniques for the hydraulic and electrical transport, we here employed LB simulations for both, which provide a more consistent basis for synthesizing permeability, formation factor and geometric attributes. The LB method has seldom been used to simulate formation factor of porous rock. The methodology we adopted here proved to be effective, but we should also note that by no means is it the only feasible approach for simulating electrical transport. For example, Chai and Shi[56] have proposed an alternative formulation by adding an additional term on the right-hand side of the evolution equation such that the Chapman-Enskog expansion in time and space would recover the exact Poisson equation when diffusivity is non-zero.

4.2. Comparison with experimental rock physics data

The 24 unit cubes have computed porosities ranging from 6.5% to 21.1%. Values of permeabilities (Figs. 3 and 7a) and formation factors (Fig. 4) inferred from LB simulations vary by less than one order of magnitude for cubes of comparable porosities, and the scatter is comparable, and may even be somewhat smaller than that of the laboratory measurements. Because Fontainebleau sandstone is not associated with appreciable bedding, laboratory samples are typically not oriented and

probably cored in random orientations. Accordingly, the scatter in laboratory data may have been due to the cooperative effect of heterogeneity and anisotropy.

As for permeability, results shown in Fig. 4 indicates that our permeability calculations is generally closer to the experimental measurements than previous numerical studies (most of which also used the LB method), especially when the porosity is below 10%. The improvement here may be attributed to several factors. First, advance in computation capability has allowed us to consider a unit cube of larger dimension, that more closely approximates a REV of the porous sandstone. Whereas we considered a sub-volume of 190^3 voxels, Arns et al.[35] started off with a sub-volume of only 120^3 voxels, and to circumvent numerical issues related to percolation in the low-porosity regime, they had to "fine grain" the CT image by replacing each voxel by $2 \times 2 \times 2$ voxels with half the linear dimension. Second, difference in the LB methodology may have contributed to the discrepancy, but in the absence of more detailed description of their numerical procedure, it is difficult to assess this issue. Lastly, difference in segmentation algorithms can also result in subtle differences in pore geometry of segmented images, which would impact permeability values derived from LB simulations.

Previous studies have used the CT images acquired and segmented by Lindquist et al.[9] For each segmented image of the four samples, Arns et al.[28] characterized its specific surface area and reciprocal (the hydraulic radius) (Fig. 6). In the current study, the original CT images acquired by Lindquist et al.[9] was segmented using a different algorithm, and it can be seen from Fig. 6 that the hydraulic radius determined from our segmented images are systematically lower than Arns et al.[28] with the implication that our segmented images had a larger specific area, likely because many fine features in the pore space had been preserved in our segmentation process. The discrepancy cannot be due to image resolution, since the two different segmentations were performed on the same CT images. As a matter of fact, our values are in good agreement with,[22] who derived their values from CT images with a somewhat coarser resolution (voxel size 7.5 μm). Our values are also comparable to NMR diffusion measurements of [53] which had a resolution of 2 μm somewhat finer than ours. In the study of [49] the microstructure was characterized using LSCM with sub-micron resolution, which can resolve refined features such as microcracks that may be missed in CT imaging. Accordingly, one expects their stereological measurements to give a somewhat larger surface area (and smaller hydraulic radius) than CT imaging. Significant ambiguity is associated with interpreting the mercury porosimetry measurement, and hydraulic radius values so inferred have significant scatter, but at least they bracket the other measurement (Fig. 6).

In our hybrid scheme, the pore-scale LB results were linked with FE simulation in a homogenized approach to compute and upscale formation factor and permeability tensor at specimen scale. White et al.[15] have demonstrated the feasibility and effectiveness of such an approach for calculating the permeability of Castlegate sandstone (with porosity of 20–24%). Our study has shown that this hybrid scheme can be extended to calculating both effective permeability and formation factor of a porous sandstone, with porosities over a relatively broad range that is associated with an appreciable change in connectivity. Like Castlegate sandstone, Fontainebleau sandstone is relatively homogeneous and isotropic; even though the FE homogenization scheme was implemented on a rather small number (8) of sub-volumes, it has provided realistic simulation of the flow fields and effective permeability (Figs. 8a, 8b, and 9) for the two more porous samples FB13 and FB22. However, due to the significant decrease of connectivity in the low-porosity regime, the flow field in FB75 (Fig. 8c) is heterogeneous and discrepancy in its permeabilities (Fig. 9) inferred from various averaging schemes suggest that the volume here may barely be representative. Indeed, the laboratory data also show more appreciable scatter in the low-porosity regime (Fig. 3), which indicate that even these cm-size samples are marginal as REV.
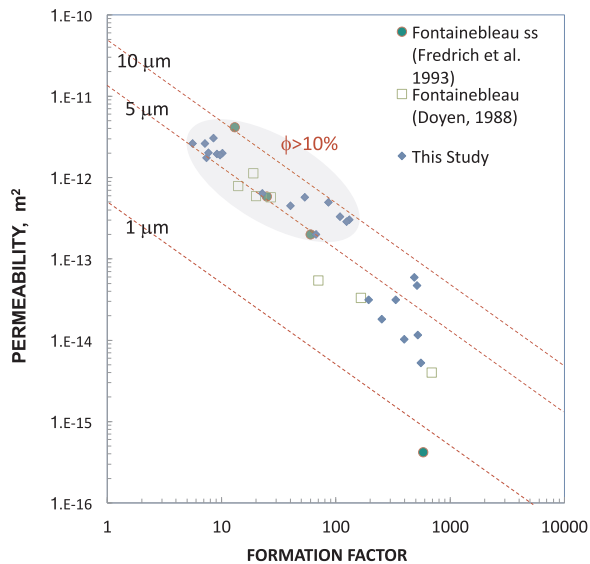
Fig. 10. Permeability of Fontainebleau sandstone as a function of formation factor. Values from our LB simulations on the 24 cubic units are shown as solid blue symbols. For comparison, laboratory measurement of Doyen[48] and Fredrich et al.[49] are also plotted. The dashed lines (of slope of unity) correspond to prediction Eq. (7) of the equivalent channel model, with geometric factor $b = 2$ and constant hydraulic radius of 1 μm, 5 μm and 10 μm, respectively. The laboratory and simulated data enclosed within the grey region are for specimens with porosities greater than 10%.

4.3. Specific surface area, hydraulic radius and characteristic length scale for transport

Laboratory data and simulated values of the transport properties indicate an overall trend for permeability to decrease (Fig. 3) and formation factor to increase (Fig. 4) with a decrease in porosity (and the corresponding increase in cementation). If these changes in transport properties derive primarily from pore size change (with negligible change in pore space connectivity), then the equivalent channel model[52,53] can provide a first-order characterization of the pore geometry. This model predicts that the mean hydraulic radius m is related to the permeability k and formation factor F as follows:

$$m = \sqrt{bkF} \qquad (7)$$

Here b is a geometric factor, with values of 2 for circular tubes and 3 for cracks, respectively. For constant hydraulic radius and geometric factor, the permeability and reciprocal of formation factor are linearly related according to (7). We plot in Fig. 10 selected laboratory data for permeability versus formation factor. Our simulated values for transport in the axial direction are also included. The measurements and simulated values for all Fontainebleau samples with porosities > 10% are enclosed within the grey region. It can be seen that, accordingly to (7), these data points are bracketed by the two lines that correspond to hydraulic radii of 5 μm and 10 μm, respectively (for geometric factor $b = 2$). In this conceptual model, transport in the high-porosity regime is controlled by "throats" in the form of cylindrical tubes with a hydraulic radius that falls in a relatively narrow range. At the higher end the average radius is comparable to values inferred from CT images and NMR measurements with resolutions of 2–5 μm, and at the lower end it is comparable to values inferred from LSCM measurements with submicron resolution.

With increase in cementation and further reduction of porosity down to 10% and below, the equivalent channel model suggests a drastic decrease of hydraulic radius to a value of as small as < 1 μm in the low-porosity regime (Fig. 10). This model prediction is in basic disagreement with all the measurements (Fig. 6), which consistently indicate at most a slight decrease of hydraulic radius in the transition

from high- to low-porosity regime. As noted by 49 the discrepancy arises from failure of the equivalent channel model to capture realistically the connectivity changes in the low-porosity regime which, according to our LM simulations, is accompanied by the development of unconnected porosity (Fig. 5) that inhibits flow and renders the overall flow field to become highly heterogeneous (Fig. 2). A key assumption of the equivalent channel model is that the flow field is relatively homogeneous, which is no longer valid in the presence of such strong heterogeneities. Our digital rock physics modeling has elucidated the heterogeneous development of flow paths that accompanies the connectivity loss. It is beyond the scope of this study to investigate in more details and quantify the concomitant evolution of geometric attributes, which can likely provide useful insights into the complex interplay of pore geometry, connectivity and transport in a porous rock.

5. Conclusion

We have developed a hybrid LB/FE computation scheme for transport properties of a porous rock that is based on a hierarchical multiscale approach. The simulated permeability and formation factor have magnitude and anisotropy that are in good agreement with experimental rock physics data. They can realistically reproduce the evolution of transport properties with porosity in Fontainebleau sandstone. Synthesis of the measured and simulated data on transport properties, connected porosity, and specific surface areas provides insights into how changes in dimensions and connectivities of the pore space control the evolution of the transport properties. By comparing measurements of geometrical attributes, formation factors and calculated permeability, we provide evidences that demonstrate the difficulties on calculating permeability for low-porosity specimens, which may help explaining the discrepancies among previous studies.

References

1. Bjørlykke K, ed. *Petroleum Geoscience, From Sedimentary Environments to Rock Physics.* Heidelberg: Springer; 2010:508.
2. Ingebritsen SE, Sanford WE, Neuzil CE. *Groundwater in Geologic Processes. 2nd ed.* New York: Cambridge University Press; 2006:536.
3. Scholz CH. *The Mechanics of Earthquakes and Faulting.* 2nd edition Cambridge: Cambridge University Press; 2002.
4. Segall P. *Earthquake and Volcano Deformation.* Princeton: Princeton University Press; 2010:432.
5. Guéguen Y, Palciauskas V. *Introduction to the Physics of Rocks.* Princeton, New Jersey: Princeton University Press; 1994:294.

6. Zinszner B, Pellerin F-M. *A Geoscientist's Guide to Petrophysics (Translated by Trevor Jones)*. Paris: Editions Technip; 2007:384.

7. Kleinberg RL. Nuclear magnetic resonance. In: Wong PZ, ed. San Diego: Academic Press; 1999:337–385. Experimental Methods in the Physical Sciences; 35.

8. Fredrich JT, Menendez B, Wong T-f. Imaging the pore structure of geomaterials. *Science.* 1995;268:276–279.

9. Lindquist WB, Venkatarangan A, Dunsmuir J, Wong T-f. Pore and throat size distributions measured from synchrotron X-ray tomographic images of Fontainebleau sandstones. *J Geophys Res.* 2000;105:21509–21527.

10. Arns CH, Knackstedt MA, Val Pinczewski W, Martys NS. Virtual permeametry on microtomographic images. *J Pet Sci Eng.* 2014;45:41–46.

11. Fredrich JT, Di Giovanni AA, Noble DR. Predicting macroscopic transport properties using microscale image data. *J Geophys Res.* 2006;111:B03201.

12. Knackstedt MA, Latham S, Madadi M, Sheppard A, Varslot T. Digital rock physics: 3D imaging of core material and correlations to acoustic and flow properties. *Lead Edge.* 2009:28–33.

13. Zhan X, Schwartz LM, Toksoz MN, Smith WC, Morgan FD. Pore-scale modeling of electrical and fluid transport in Berea sandstone. *Geophysics.* 2010;75:F135–F142.

14. Louis L, Wong T-f, Baud P, Tembe S. Imaging strain localization by X-ray computed tomography: discrete compaction bands in Diemelstadt sandstone. *J Struct Geol.* 2006;28(5):762–775.

15. White JA, Borja RI, Fredrich JT. Calculating the effective permeability of sandstone with multiscale lattice Boltzmann/finite element simulations. *Acta Geotech.* 2006;1:195–209.

16. Sun WC, Andrade JE, Rudnicki JW. Multiscale method for characterization of poous microstructures and their impact on macroscopic effective permeability. *Int J Num Methods Eng.* 2011;88:1260–1279.

17. Charalampidou E-M, Hall SA, Stanchits, Lewis SH, Viggiani G. Characterization of shear and compaction bands in a porous sandstone deformed under triaxial compression. *Tectonophysics.* 2011;503:8–17.

18. Ji Y, Hall SA, Baud P, Wong T-f. Characterization of pore structure and strain localization in Majella limestone by X-ray computed tomography and digital image correlation. *Geophys J Int.* 2005;200:699–717.

19. Wang K, Sun WC. A semi-implicit discrete-continuum coupling method for porous media based on the effective stress principle at finite strain. *Comput Methods Appl Mech Eng.* 2016;304:546–583.

20. Wang K, Sun WC W, Salager S, Na S, Khaddour G. Identifying material parameters for a micro-polar plasticity model via X-ray micro-computed tomographic (CT) images: lessons learned from the curve-fitting exercises. *Int J Multiscale Comput Eng.* 2016;14(4):389–413.

21. Spanne P, Thovert JF, Jacquin CJ, Lindquist WB, Jones KW, Adler PM. Sychrotron computer microtomography of porous media: topology and transports. *Phys Rev Lett.* 1994;73:2001–2004.

22. Auzerais FM, Dunsmuir J, Ferreol BB, et al. Transport in sandstone: a study based on three dimensional microtomography. *Geophys Res Lett.* 1996;23:705–708.

23. Thiry M, Ayrault MB, Grisoni J-C. Groundwater silicification and leaching in sands: examples of the Fontainebleau sand (Oligocene) in the Paris basin. *Geol Soc Am Bull.* 1998;100:1283–1290.

24. Jacquin CG. Correlations entre la permeabilite et les caracteristiques geometriques du gres de Fontainebleau. *Oil Gas Sci Technol.* 1964;19(7–8):921–937.

25. Bourbie T, Zinszner B. Hydraulic and acoustic properties as a function of porosity in Fontainebleau Sandstone. *J Geophys Res.* 1985;90:11524–11532.

26. Zhu W, David C, Wong T-f. Network modeling of permeability evolution during cementation and hot isostatic pressing. *J Geophys Res.* 1995;100:15451–15464.

27. Mavko G, Nur A. The effect of a percolation threshold in the Kozeny-Carman relation. *Geophysics.* 1997;62:1480–1482.

28. Arns CH, et al. Digital core laboratory: petrophysical analysis from 3D imaging of reservoir core fragments. *Petrophysics.* 2005;46(4):260–277.

29. Gomez CT, Dvorkin J, Vanorio T. Laboratory measurements of porosity, permeability, resistivity, and velocity on Fontainebleau sandstones. *Geophysics.* 2010;75:E191–E204.

30. Bernabé Y, Zamora M, Li M, Maineult A, Tang YB. Pore connectivity, permeability, and electrical formation factor: a new model and comparison to experimental data. *J Geophys Res: Solid Earth.* 2011;116(B11).

31. Andrä H, et al. Digital rock physics benchmarks, II computing effective properties. *Comput Geosci.* 2013;50:33–43.

32. Lock PA, Jing XD, Zimmerman RW, Schlueter EM. Predicting the permeability of sandstone from image analysis of pore structure. *J Appl Phys.* 2002;92:6311–6319.

33. Lock PA, Jing XD, Zimmerman RW. Comparison of methods for upscaling permeability from the pore scale to the core scale. *J Hydraul.* 2004;42:3–8.

34. Arns CH, Knackstedt MA, Val Pinczewski W, Lindquist WB. Accurate estimation of transport properties from microtomographic images. *Geophys Res Lett.* 2001;28:3361–3364.

35. Arns CH, Knackstedt MA, Val Pinczewski W, Martys NS. Virtual permeametry on-microtomographic images. *J Pet Sci Eng.* 2004;45(1–2):41–46.

36. Thovert J-F, Yousefian F, Spanne P, Jacquin CG, Adler P. Grain reconstruction of porous media: application to a low-porosity Fontainebleau sandstone. *Phys Rev, E.* 2011;63:061307.

37. Sun WC, Andrade JE, Rudnicki JW, Richhubl P. Connecting microstructural attributes and permeability from 3D tomographic images of in situ shear-enhanced compaction bands using multiscale computations. *J Geophys Res.* 2011;38:L10302.

38. Ridler TW, Calvard S. Picture thresholding using an iterative selection method. *IEEE Trans Syst, Man Cybern.* 1978;8:630–632.

39. Ohser J, Muecklich F. *Statistical Analysis of Microstructures in Material Sciences.* John Wiley and Sons; 2000.

40. Legland D, Kiêu K, Devaux M-F. Computation of Minkowski measures on 2D and 3D binary images. *Image Anal Stereol.* 2007;26:83–92.

41. Zou Q, He X. On pressure and velocity boundary conditions for the lattice Boltzmann BGK model. *Phys Fluids.* 1997;9(6):1591–1598.

42. Narváez Salazar AE, Harting JDR. Evaluation of pressure boundary conditions for permeability calculations using the lattice-Boltzmann method. *Adv Appl Math Mech.* 2010;2(5):685–700.

43. Wolf-Gladrow D. A lattice Boltzmann equation for diffusion. *J Stat Phys.* 1995;79:1023–1032.

44. Haslam IW, Crouch RS, Seaïd M. Coupled finite element–lattice Boltzmann analysis. *Comput Methods Appl Mech Engrg.* 2008;197:4505–4511.

45. Sun WC, Kuhn MR, Rudnicki JW. A multiscale DEM-LBM analysis on permeability evolutions inside a dilatant shear band. *Acta Geotech.* 2013;8(5):465–480.

46. Shan X, Doolen G. Diffusion in a multicomponent lattice Boltzmann equation model. *Phys Rev, E.* 1996;54:3614–3620.

47. David C. Geometry of flow paths for fluid transport in rocks. *J Geophys Res.* 1993;98(B7):12267–12278.

48. Doyen PM. Permeability, conductivity, and pore geometry of sandstone. *J Geophys Res.* 1988;93:7729–7740.

49. Fredrich JT, Greaves KH, Martin JW. Pore geometry and transport properties of Fontainebleau sandstone. *Int J Rock Mech Min Sci.* 1993;30:691–697.

50. David C, Darot M. Permeability and conductivity of sandstones. In: Maury V, Fourmaintraux D, eds. *Rock at Great Depth.* Rotterdam: A. A. Balkema; 1989:203–209.

51. Kieffer B, Jové CF, Oelkers EH, Schott J. An experimental study of the reactive surface area of the Fontainebleau sandstone as a function of porosity, permeability, and fluid flow rate. *Geochim Cosmochim Acta.* 1999;63:3525–3534.

52. Paterson MS. The equivalent channel model for permeability and resistivity in fluid-saturated rocks: a re-appraisal. *Mech Mater.* 1983;2:345–352.

53. Walsh JB, Brace WF. The effect of pressure on porosity and the transport properties of rock. *J Geophys Res.* 1984;89:9425–9431.

54. Hürlimann MD, Helmer KG, Latour LL, Sotak CH. Restricted diffusion in sedimentary rocks. determination of surface-area-to-volume ratio and surface relaxivity. *J Magn Reson A.* 1994;111:169–178.

55. Clavaud J-B, Maineult A, Zamora M, Rasolofosaon P, Schlitter C. Permeability anisotropy and its relations with porous medium structure. *J Geophys Res.* 2008;113:B01202.

56. Chai Z, Shi B. A novel lattice Boltzmann model for the Poisson equation. *Appl Math Model.* 2008;32:2050–2058.